https://doi.org/10.1007/s41230-026-5181-7

Drop-weight impact resistances of integrated forming aluminum foam sandwich double tubes

Xin-pei Xu[1], Zan Zhang[2], **Jian Ding[1], Li-peng Cui[1], Zi-xuan Qiu[1], Yong Li[1], Peng-wei Chen[1], ***Zi-chen Zhang[3], Bo-xiao Liu[1], and *Xing-chuan Xia[1]

1. School of Material Science and Engineering, Hebei University of Technology, Tianjin 300130, China

2. School of Physics and Electronic Engineering, Xing Tai University, Xingtai 054001, Hebei, China

3. Suzhou Laboratory, Suzhou 215100, Jiangsu, China

Copyright © 2026 Foundry Journal Agency

Abstract: Aluminum foam filled tubes are good energy-absorbing structures. In this study, integrated forming aluminum foam sandwich double tubes (IFAFSDTs) were fabricated utilizing an improved melt foaming method to achieve superior metallurgical bonding between foam core and inner/outer tubes, which is a critical advancement over traditional mechanically assembled counterparts. The preparation process, mechanical properties under axial impact, energy absorption capacity, and deformation failure mechanism of IFAFSDTs were investigated. Results indicate that holding temperature is crucial for the metallurgical bonding and the optimal holding temperature is 410 °C. The mechanical properties and energy absorption performance of IFAFSDTs under the optimal condition were investigated through drop-weight impact tests, with specific focusing on the effect of diameter ratio (R) and aspect ratio (L) of IFAFSDTs. IFAFSDTs with R of 0.35 and IFAFSDTs with L of 1.25 exhibit the highest energy absorption capacity at a specific strain, and sustain the peak crushing forces of 283 kN and 244 kN, respectively. During impact process, the outer tube undergoes an axisymmetric circular ring symmetric buckling mode, while the inner tube exhibits an asymmetric diamond mode. Energy absorption modes of aluminum foam core include pore structure deformation and collapse, grain deformation, and intergranular fracture. Due to the different extent of deformation in different regions of the aluminum foam core, the dominant energy absorption mode changes in each region and the microstructure after impact shows obvious differences.

Keywords: integrated forming aluminum foam sandwich double tubes (IFAFSDTs); metallurgical bonding; axial impact resistance; energy absorption

CLC numbers: TG146.21 **Document code:** A **Article ID:** 1672-6421(2026)03-435-16

1 Introduction

Aluminum foam is a porous metallic material composed of aluminum or aluminum alloy matrix with a substantial volume of internal pores. These pores can be either closed (closed-cell foam) or interconnected (open-cell foam), leading to significantly different properties and applications. Compared with open-cell aluminum foam, closed-cell aluminum foam has higher strength, lower density, excellent energy absorption capacity, and stable deformation modes, is extensively utilized in the field of energy absorption and shock mitigation[1, 2]. The most common techniques to manufacture aluminum foams include melt foaming method, powder metallurgy route, and gas injection method[3].

Aluminum foam is commonly utilized as filling material to improve the energy absorption and buffer capacity of the whole structure[4]. Aluminum foam-filled tubes (FFTs) represent a typical composite structure, characterized by solid metal outer layer and an aluminum foam core[5, 6]. Due to the inherent advantages of aluminum foam and solid metal tubes, as well as their synergistic interaction, the yield strength and deformation stability of FFTs are significantly improved, exhibit exceptional energy absorption performance and load carrying capabilities[7, 8]. Nevertheless, its specific energy absorption falls short compared to that of the corresponding hollow tubes[9, 10].

***Xing-chuan Xia**

Male, born in 1981, Ph. D., Researcher. His research interests mainly focus on the integrated preparation and performance evaluation of metallic foam.

E-mail: xiaxingchuan0101@163.com

****Jian Ding**

E-mail: djian0122@126.com

*****Zi-chen Zhang**

E-mail: zhangzc@szlab.ac.cn

Received: 2025-08-04; Revised: 2025-09-09; Accepted: 2025-11-04

Therefore, in order to further enhance energy absorption efficiency and mechanical properties of FFTs, novel composite structure aluminum foam sandwich double tubes (AFSDTs) were proposed[11, 12]. This structure generally comprises inner and outer layers of solid metal, as well as a middle layer of aluminum foam core. Researchers have demonstrated that this structure exhibits a significant improvement of overall crashworthiness and energy absorption efficiency compared to those of both the double hollow tubes and the single tube filled with metal foams[13, 14]. Consequently, it represents an efficient and stable energy absorption component with significant potential for impact protection applications.

AFSDTs can be fabricated through two typical methods: secondary processing method and integral forming technique. The secondary processing method involves initially cutting aluminum foam and solid metal tubes to the required dimensions, followed by bonding the two components using adhesives, brazing, or mechanical fastening. This method is characterized by its straightforward fabrication principle and is currently the most widely employed approach for producing aluminum foam-filled structures[15]. However, aluminum foam-filled structures fabricated via the secondary processing method often exhibit several limitations, including low interfacial bonding strength, high density and susceptibility to damage during processing[16, 17]. The integral forming method enables the simultaneous achievement of foam formation in aluminum foam core and the metallurgical bonding at the interface between aluminum foam core and solid metal tubes[18]. Since the strength of the interfacial metallurgical bonding significantly influences the mechanical properties of aluminum foam-filled structures[19, 20], the integral forming method offers distinct advantages. The melt foaming method is a highly promising integral forming technique due to its simple process flow and suitability for preparing large-sized samples. However, the preparation of AFSDTs using the melt foaming method presents considerable challenges, primarily due to the confined foaming space in AFSDTs and the limited heat dissipation conditions of the inner tube.

Previous studies have demonstrated that inner and outer tubes of AFSDTs play a crucial role in guiding and controlling the deformation of metal foam core[21, 22]. The foam core of this structure significantly improves the overall energy absorption performance, with the magnitude of this enhancement being dependent on the filling density[23]. Foam-filled sandwich double tubes exhibit superior energy absorption characteristics and deformation resistance when compared to single-tube counterparts[24, 25]. Furthermore, the height of the aluminum foam-filled structure has been identified as a critical factor influencing load fluctuation and energy absorption capacity[26]. In addition, the majority of previous studies has predominantly focused on specimens fabricated through secondary processing methods. Limited attention has been given to the impact resistance of AFSDTs manufactured via integral forming processes. Notably, these AFSDTs, featuring metallurgical bonding interfaces achieved by intergral forming processes, present substantial potential for applications in energy absorption and buffering systems.

In this study, an improved melt foaming method was employed to fabricate integrated forming aluminum foam sandwich double tubes (IFAFSDTs) with varying heights and inner tube diameters. The influence of holding temperature on metallurgical bonding between aluminum foam core and inner/outer aluminum alloy tubes was systematically studied. Through axial drop weight impact tests, the effects of diameter ratio (R) and aspect ratio (L) of IFAFSDTs on the axial impact resistance and energy absorption performance were evaluated, and compared with the experimental results of FFTs prepared by other methods. Deformation modes and failure mechanisms of IFAFSDTs during axial impact process were thoroughly investigated through detailed analysis of their deformation processes. The energy absorption mechanism of IFAFSDTs during the impact process was also analyzed.

2 Materials and methods

2.1 Specimen preparation

IFAFSDTs were fabricated using an improved melt foaming method, which separated processes of melt heating and mold insulation in upper and lower regions of the furnace, as shown in Fig. 1. Compared with traditional melt foaming method, the improved melt forming method offers more precise temperature control and shortens the pouring time, optimizing the thickening and foaming processes. 6063 aluminum alloy tubes were selected as inner and outer tubes. Pure aluminum ingots (Al, with purity of 99.5wt.%) were selected as matrix metal. TiH_2 powders (commercially pure, 300±20 mesh) were used as foaming agent. TiH_2 decomposed at temperatures above 490 °C[27], ensuring gas released when the metal was in molten state. Magnesium ingots (Mg, with purity of 99.5wt.%) were used as wetting agent, which can effectively regulate the surface tension of the melt, making the shape of the pores closer to spherical[28]. Calcium granules (Ca, commercially pure, granularity between 1.0 and 2.5 mm) were added as thickening agent to increase the viscosity, which is crucial for stabilizing bubbles and preventing cell wall rupture[29]. Based on literature review and preliminary experiments, the addition amount of TiH_2 in this study was 1.5wt.% with stirring speed of 1,200 $r \cdot min^{-1}$, which can obtain uniform pore structures[4, 30, 31]. The contents of Mg and Ca were fixed at 1.0wt.% and 2.0wt.%, respectively with stirring speed of 400 $r \cdot min^{-1}$ based on previous work[4, 30].

The schematic diagram of the fabrication process is shown in Fig. 1. The specific preparation process is as follows: (1) melting about 1 kg pure aluminum at 690 °C; (2) adding Mg into the melt then stirring for 4 min under speed of 400 $r \cdot min^{-1}$; (3) adding Ca particles and stirring for 6 min under speed of 400 $r \cdot min^{-1}$; (4) adding TiH_2 powders and stirring for 10 s under the speed of 1,200 $r \cdot min^{-1}$; (5) pouring foaming melt from the crucible into the mold within 10 s and holding for 3–5 min at different temperatures for sufficient gas release and pore growth, then taking out the mold and cooling

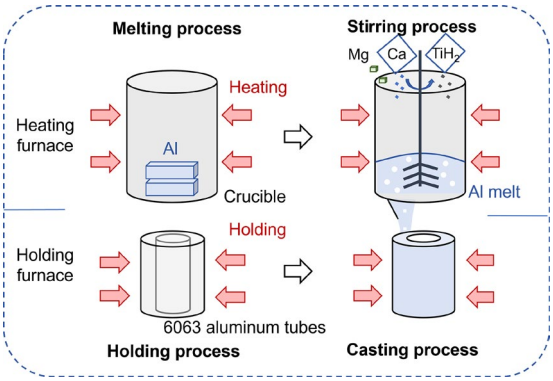

Fig. 1: Schematic diagram of fabrication process

naturally for about 1 h. The equipment used for preparation was a self-designed double-layer resistance furnace with both heating and isothermal holding functions.

The metallurgical bonding between aluminum foam core and tubes is crucial for the overall structural strength and impact resistance[32]. The effect of holding temperature (330 °C, 370 °C, 410 °C, 450 °C, and 490 °C) on metallurgical bonding of interface was investigated with the foaming stirring temperature fixed at 690 °C.

The diameter ratio (R) is defined as the ratio of the inner diameter to the outer diameter of the IFAFSDTs, and the aspect ratio (L) is defined as the ratio of the sample height to 60 mm. To systematically investigate the effect of R and L on impact resistance, IFAFSDTs with a fixed outer diameter of 60 mm but various R and L were fabricated. For a fixed height of 60 mm, inner tube diameters of 27 mm, 21 mm, and 15 mm corresponded to R values of 0.45, 0.35, and 0.25. For a fixed inner tube diameter of 27 mm, sample heights of 60 mm, 75 mm, and 90 mm corresponded to L values of 1, 1.25, and 1.5, respectively. The thickness of both inner and outer tubes was 1.5 mm. For each set of parameters, three samples were prepared to ensure reproducibility of experiments and the average values were recorded.

2.2 Pore structure analysis

To accurately characterize the pore size distribution, porosity, and circularity of IFAFSDTs, the pore structure in both cross-section and longitudinal-section was comprehensively analyzed. Images of the horizontal and vertical symmetry planes of IFAFSDTs were selected and processed using ImageJ software for binarization, as illustrated in Fig. 2. By statistically evaluating the pore structural characteristics in Regions 1, 2a, and 2b, and applying Eqs. (1)–(3) for calculation, the overall pore size distribution D_E, porosity P_E, and circularity C_E of IFAFSDTs were determined. D_1, D_{2a}, and D_{2b} represent the distribution frequency of pore sizes in Regions 1, 2a, and 2b, respectively. P_1, P_{2a}, P_{2b} and C_1, C_{2a}, C_{2b} denote the average porosity and average circularity in these three regions.

$$D_E = D_1 \times 50\% + (D_{2a} + D_{2b}) \times 50\% \quad (1)$$

$$P_E = P_1 \times 50\% + (P_{2a} + P_{2b}) \times 50\% \quad (2)$$

$$C_E = C_1 \times 50\% + (C_{2a} + C_{2b}) \times 50\% \quad (3)$$

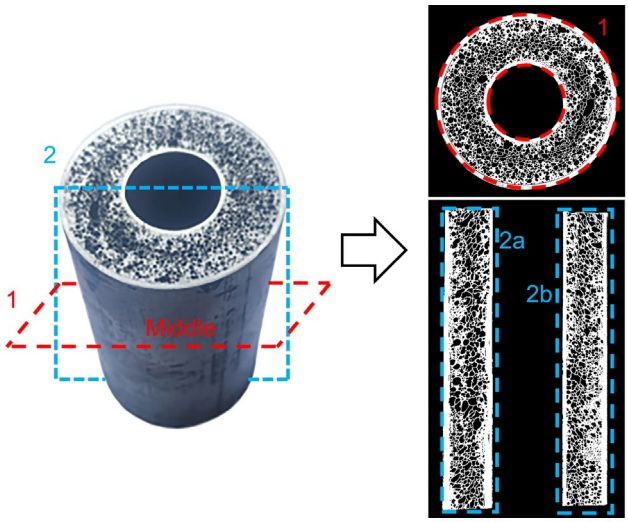

Fig. 2: Statistical method for pore structure

2.3 Drop-weight impact test

Drop weight impact tests were conducted to investigate the axial impact resistance of IFAFSDTs. Related testing method has been reported in authors' previous research[33]. The impact body consisted of a drop hammer and a counterweight, with a total mass of 104.7 kg. The initial vertical height of the drop hammer was 4 m. The impact force, impact action time, and vertical deformation displacement were recorded during drop-weight impact test. In addition, several key parameters were selected for further evaluating the axial impact resistance performance of IFAFSDTs. Peak crushing force (F_{PC}) is the first peak stress in impact force-displacement curve. Total energy absorption (E_A) can be expressed by Eq. (4)[34]:

$$E_A = \int_0^{\delta} F(x)\,\mathrm{d}x \quad (4)$$

where x is axial compression displacement of sample after the impact body contacts IFAFSDTs, δ represents the maximum displacement and $F(x)$ represents the impact force when axial displacement is x. In addition, energy absorption capacity (W) represents the energy absorption per unit volume of the specimen, which can be calculated by Eq. (5)[35]:

$$W = \int_0^{\tau} \sigma(\varepsilon)\,\mathrm{d}\varepsilon \quad (5)$$

where ε is axial compression strain of sample, τ represents the maximum strain and $\sigma(\varepsilon)$ represents the stress value when strain is ε. Besides, mean crushing force (F_{MC}) is the ratio of total energy absorption to effective impact deformation displacement, as shown in Eq. (6)[36]:

$$F_{MC} = \frac{E_A}{\delta} \quad (6)$$

Peak stress and mean stress are obtained through dividing peak crushing force and mean crushing force by the stress area of the specimen. The undulation of load-carrying capacity (U_{LC}) is defined as the ratio of the work done by the specimen deviating from the mean crushing force to the total energy absorption during the impact process. It reflects the amplitude of impact force variation of the specimen during testing process[37] and can be calculated using Eq. (7). A lower U_{LC}

value indicates a reduced amplitude of load fluctuations.

$$U_{LC}=\frac{\int_0^{\delta}|F(x)-F_{MC}|\,dx}{E_A} \quad (7)$$

2.4 Finite element simulation

Finite element (FE) simulation of the drop-weight impact process of IFAFSDTs was conducted using ABAQUS software. The FE model consisted of an IFAFSDT, a drop hammer, and a support panel, as shown in Fig. 3. The model of IFAFSDT was obtained by reconstructing micro computed X-ray tomography scanning images (Sanying Precision Instruments Co., Ltd., Tianjin, China) using Avizo software (Thermo Fisher Scientific, USA, Tianjin Sanying Precision Instrument Co., Ltd.). The Johnson-Cook model was used to describe the deformation behavior of the matrix alloy Al-Ca-Ti-Mg. Assuming that the alloy hardens isotropically, without considering true strain and temperature, the relationship between flow stress σ and equivalent plastic strain ε can be expressed as:

$$\sigma=(A+B\varepsilon^n)(1-C\ln\dot{\varepsilon}^*) \quad (8)$$

where $\dot{\varepsilon}^*$ is the dimensionless strain rate, A is the yield strength, B represents strain strengthening modulus, n is strain hardening coefficient, and C presents the strain rate sensitivity coefficient. Specific constitutive parameters were obtained by substituting experimental data into the solution and are listed in Table 1.

In ABAQUS, the contact interaction between the hammer and the sample, as well as between the sample and the support, was defined as surface-to-surface contact. The contact caused by the deformation and collapse of cell walls was defined as self-contact. The bottom of the sample was bound to the support using a rigid body constraint. The impact process was simulated using a dynamic/explicit modules, with the impact load was simulated by applying an initial velocity to the hammer through a predefined velocity field.

Table 1: Constitutive parameters of Johnson-Cook model of Al-Ca-Ti-Mg alloy

A (MPa)	*B* (MPa)	*n*	*C*
82.354	153.4968	0.5650	0.0049

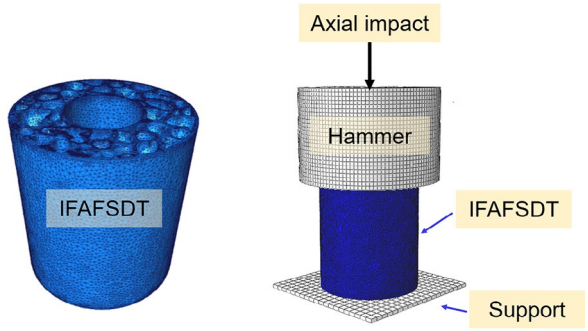

Fig. 3: FE model of drop-weight impact process of IFAFSDTs

3 Results and discussion

3.1 Interface metallurgical bonding situation

Figure 4 shows the interface bonding of IFAFSDTs prepared at holding temperatures of 330 °C, 370 °C, 410 °C, 450 °C, and 490 °C. Experimental results prove that the holding temperature is crucial for achieving a metallurgical bonding of the interface. When the holding temperature is 330 °C, metallurgical bonding between aluminum foam core and outer tube is not achieved. When holding temperature rises to 370 °C, although the macroscopic combination of aluminum foam core and inner/outer tubes is achieved, there still exists a clear boundary according to SEM images shown in Fig. 5. The interfaces between aluminum foam core and inner/outer tubes are marked with red dotted line. This is attributed to the low holding temperature (330 °C and 370 °C) which causes the melt in contact with the wall of aluminum alloy tube to solidify rapidly and hinders the metallurgical bonding at the interface. Moreover, the porosity of the specimen is low and the pore size in the bottom region of IFAFSDTs is small. When holding temperature is 410 °C, a good metallurgical bond is achieved according to SEM images. This is because high-temperature aluminum foam melt has excellent fluidity and can fully wet the wall of aluminum alloy tubes[38]. When holding temperature is relatively high, the mutual diffusion of atoms in melt and in the surface of aluminum tube results in the formation of metallurgical bonding. According to fabrication results, the sample prepared at a holding temperature of 410 °C exhibits higher porosity and thinner cell walls compared to those prepared at 330 °C and 370 °C[39]. Under holding temperature of 450 °C, the metallurgical combination is also achieved, but the inner tube locally deformation is observed after longitudinally cutting the sample. Some concentrated large holes appear in the foam core. When holding temperature reaches 490 °C, inner tube is severely deformed. This is because the holding temperature is too high, and the heat dissipation space of

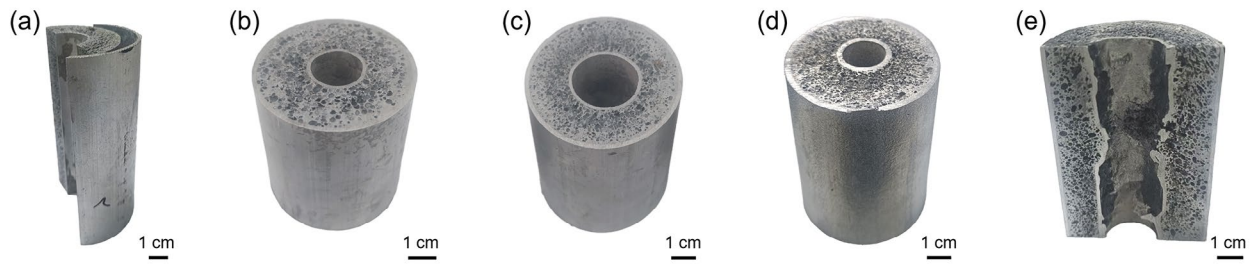

Fig. 4: Influence of holding temperature on combination of interface: (a) 330 °C; (b) 370 °C; (c) 410 °C; (d) 450 °C; (e) 490 °C

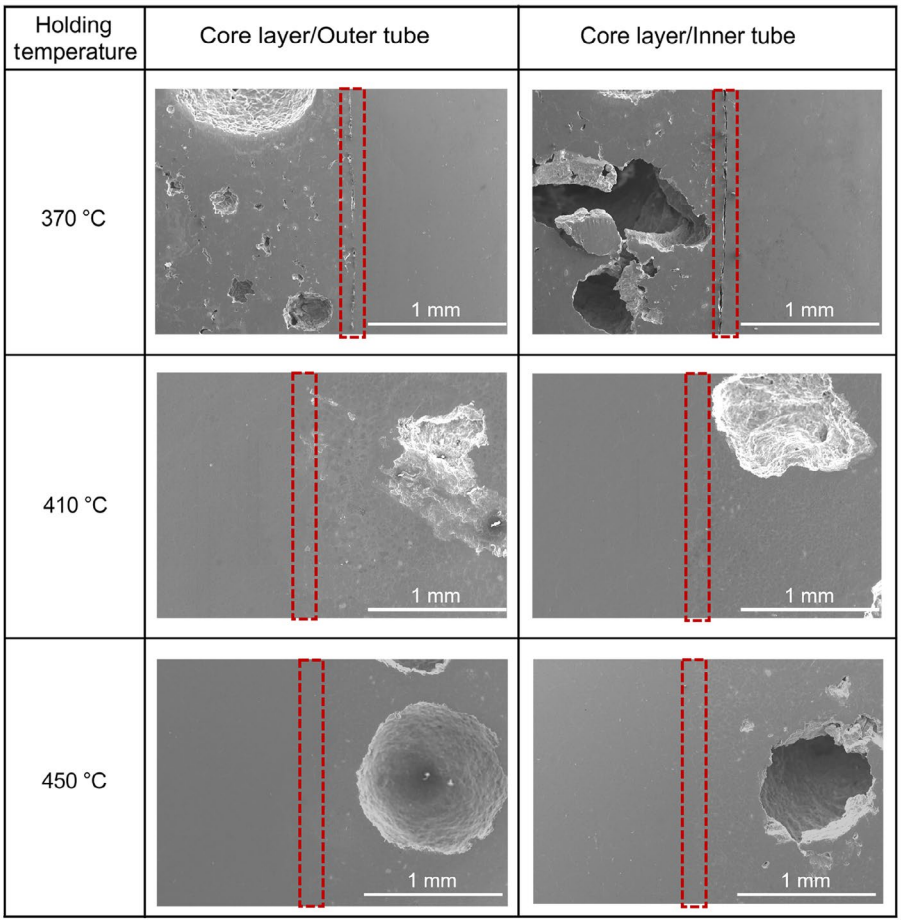

Fig. 5: Effect of holding temperatures on interface metallurgical bonding

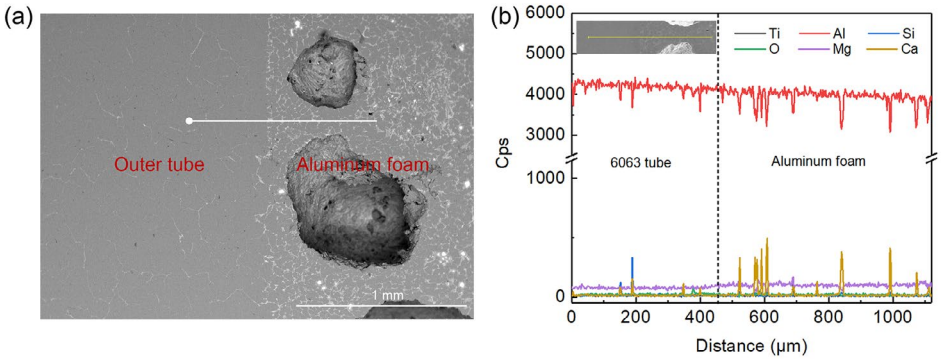

Fig. 6: BSE image (a) and EDS line scan result (b) of bonding interface under holding temperature of 410 °C

inner tube is limited, resulting in melting and deformation of the inner tube. Besides, the aluminum foam core has more concentrated large cells and the pore size distribution is not uniform. Therefore, a holding temperature of 410 °C is more desirable for the preparation of IFAFSDTs.

Based on BSE image and EDS line scanning results in Fig. 6, the interfacial metallurgical bonding of the sample prepared at a holding temperature of 410 °C is further verified. It is evident that no abrupt changes in elemental contents are observed at the interface. Subsequently, inner/outer aluminum alloy tube is separated from aluminum foam core. As shown in Fig. 7, after the IFAFSDTs are separated, aluminum foam debris remain on the wall of the aluminum alloy tube. The above experiments sufficiently demonstrate that the metallurgical bonding is formed between the foam aluminum core and inner/outer tubes.

3.2 Pore structure

To ensure a consistent pore structure in samples, the holding temperature of 410 °C, along with the holding time, pouring time, and cooling time, are strictly controlled[40, 41]. An IFAFSDT with a height of 60 mm and an inner diameter of 21 mm was selected as the typical sample. A typical pore structure distribution is illustrated in Fig. 8. The diameter of pores (D) in Regions 1, 2a, and 2b, as well as the entire sample, conforms to normal distribution, following D-N(0.79, 0.50^2), D-N(0.89, 0.63^2), D-N(0.80, 0.55^2), and D-N(0.81, 0.54^2), respectively. Majority of pore sizes in samples are concentrated in the range of 0.5–1.5 mm, with a few concentrated large pores. The porosities in Regions 1, 2a, 2b, and the entire sample are 63.1%, 62.2%, 61.6%, and 62.5%, respectively. The

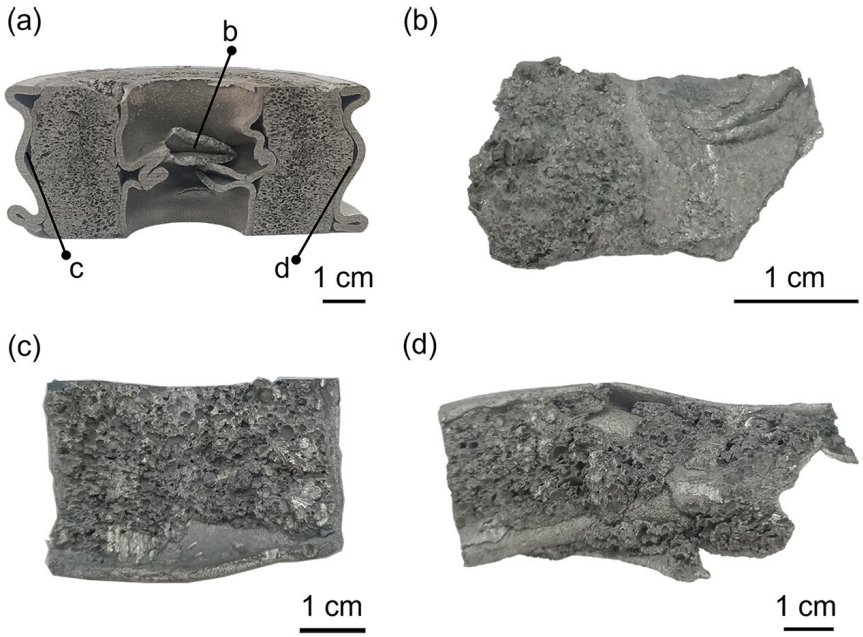

Fig. 7: Interface morphology after IFAFSDTs were separated: (a) observation area; (b) inner tube; (c) and (d) outer tube

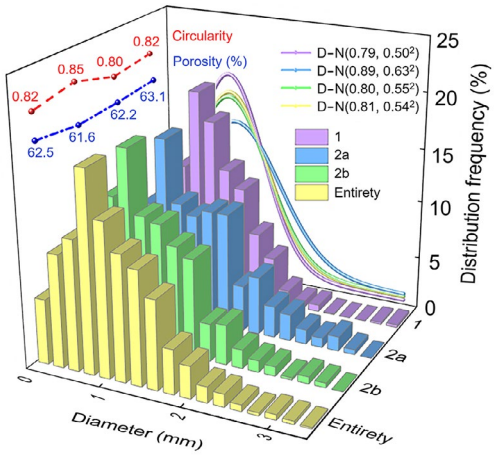

Fig. 8: Distribution of pore size, porosity, and circularity in Regions 1, 2a, 2b, and the entire sample

circularities are relatively high and similar in all four statistical regions, with values of 0.82, 0.80, 0.85, and 0.82, respectively, which is beneficial for improving the mechanical properties[42]. This is because that during the integrated preparation, the temperature in holding and cooling processes is uniform and accurately controlled, allowing bubbles to grow, evolve, and solidify uniformly within the mold cavity. Finally, IFAFSDTs exhibit uniform distribution of pore size, similar porosity and circularity. Furthermore, their small average pore size is conducive to improving the comprehensive performance[43].

3.3 Effect of diameter ratio on drop weight impact resistance

Figure 9(a) presents the axial deformation displacement of IFAFSDTs under drop weight impact with the same height of 60 mm and R values of 0.25, 0.35, and 0.45. As R increases, the axial displacement initially decreases and subsequently increases, indicating that the increase in inner tube diameter and reduction in aluminum foam filling cause the stiffness of IFAFSDTs to first increase and then decrease[44]. Figures 9(b)–(d) show the force-displacement curves for specimens with varying R. The impact force-displacement curves can be divided into three stages[45, 46]: (I) linear elastic stage, (II) progressive buckling stage, and (III) unloading stage. Observations indicate that IFAFSDTs exhibit load fluctuations within a certain range over an extended period when subjected to axial impact, signifying a stable impact resistance mechanism[47]. As R increases, the duration of impact force and vertical deformation displacement initially decreases before ascending, whereas the peak crushing force escalates from 252 kN to 283 kN before descending to 230 kN. Similarly, the mean crushing force increases from 150 kN to 171 kN, then decreases to 137 kN. Compared with composite aluminum foam filled tubes (CAFTs) without inner tube, the peak load of IFAFSDTs appears later, and the impact force fluctuation in progressive buckling stage is smaller, which indicates that its load bearing process is more stable[30, 33].

Figure 10 illustrates the effect of R on the total absorbed energy and energy absorption capability of IFAFSDTs. As R increases, the energy absorption performance first increases and then decreases. Under the same deformation displacement and strain, IFAFSDTs with R=0.35 have the highest total energy absorption. With a deformation displacement of 20 mm, the specimens with R=0.25, 0.35, and 0.45 absorb total impact energies of 2,930 J, 3,435 J, and 2,713 J, respectively. When strain is 0.3, the energy absorption capacity of the specimens with R=0.25, 0.35, and 0.45 is 33.9 MJ·m^{-3}, 43.3 MJ·m^{-3}, and 35.8 MJ·m^{-3}, respectively. Consequently, IFAFSDTs with R of 0.35 demonstrate the superior axial impact resistance.

The load-carrying capacity is a key parameter for evaluating the crashworthiness of IFAFSDTs[48]. Smaller load-carrying capacity corresponds to a smoother load fluctuation under impact loads[49]. Figure 11(a) illustrates the effect of R on the load-carrying capacity of IFAFSDTs. Upon initial contact

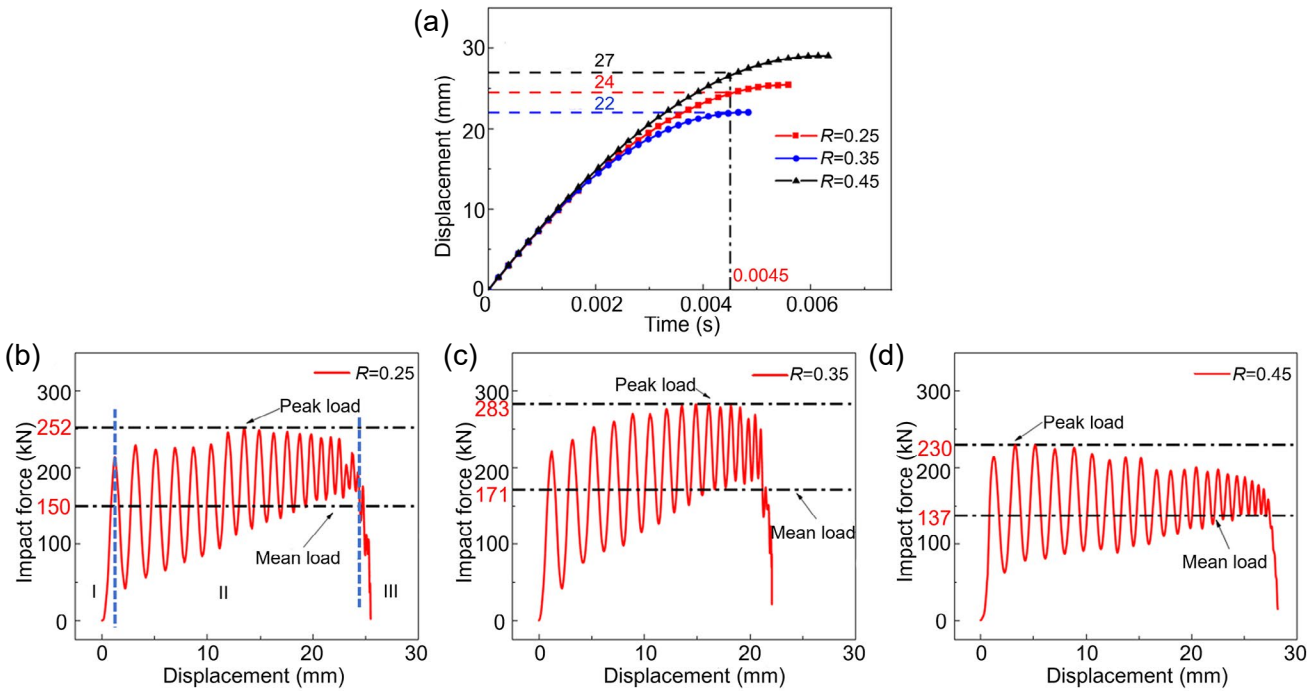

Fig. 9: Effect of *R* on deformation displacement and impact force of IFAFSDTs: (a) displacement-time curves; (b)–(d) impact force-displacement curves

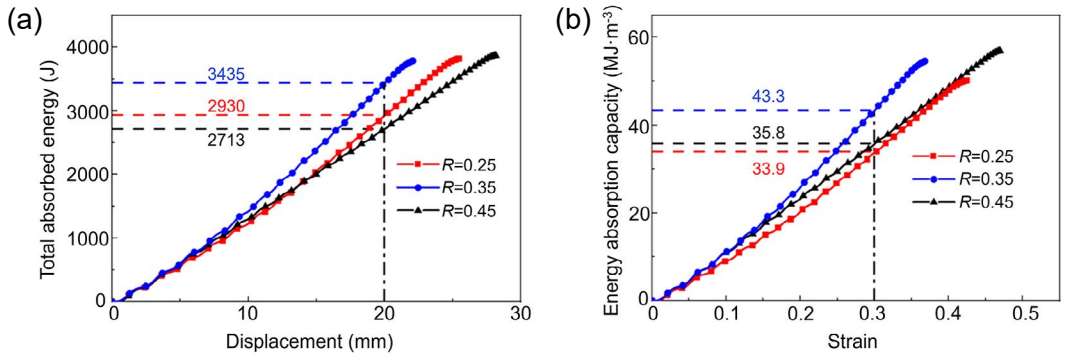

Fig. 10: Effect of *R* on energy absorption performance of IFAFSDTs: (a) total energy absorption; (b) energy absorption capacity

with hammer, all specimens exhibit obvious load fluctuations, representing the primary stage of energy absorption. Subsequently, as the impact process advances, these load fluctuations gradually diminishes. The specimen with R=0.25 exhibits the highest load-carrying capacity during the impact process.

The effect of R on the deformation velocity of IFAFSDTs is shown in Fig. 11(b). When the deformation displacement is 20 mm, the deformation velocity of three specimens is 4.12 m·s^{-1}, 2.85 m·s^{-1} and 5.20 m·s^{-1}, which is reduced by 53.4%, 67.8%, and 41.2%, respectively compared to the initial impact velocity. Specimen with R=0.35 demonstrates superior kinetic energy absorption capacity, effectively reducing the speed of impact bodies. Figure 11(c) illustrates the effect of R on the deformation acceleration of IFAFSDTs. The specimen with R of 0.35 exhibits the highest peak acceleration, suggesting superior structural strength[51]. The sample with R of 0.45 demonstrates a consistently lower peak acceleration throughout the impact process. A lower peak acceleration and fluctuation amplitude of crash protection structures can effectively mitigate injuries to personnel or damage to items[52]. Increasing R leads to the increase of the contact area between inner tube and the foam core, which improves load transfer efficiency between the foam core and tubes. This results in better collaborative deformation capability. However, when R becomes excessively large, the filling amount of aluminum foam is substantially reduced, reducing the energy absorption capacity of IFAFSDTs. Therefore, under the same displacement or strain, IFAFSDTs with R=0.35 have the best impact resistance performance.

Compared with CAFTs, IFAFSDTs with the same R value (0.25 and 0.45) exhibit better deceleration effects under the same deformation displacement. Furthermore, IFAFSDTs have higher deformation acceleration and smoother fluctuations, indicating that IFAFSDTs serve as more effective better impact protection structures[33].

3.4 Effect of aspect ratio on drop-weight impact resistance

Figure 12(a) presents the axial deformation displacement of IFAFSDTs with L values of 1, 1.25, and 1.5. The axial displacement decreases first and then increases with the increase of L. This indicates that the stiffness of specimen

initially increases and then decreases[53]. The corresponding impact force-displacement curves for specimens with varying L are illustrated in Figs. 12(b)–(d), which still comprise linear elastic stage, progressive buckling stage, and unloading stage. The peak crushing force initially increases from 230 kN to 244 kN, followed by a subsequent reduction to 168 kN with increasing L. Similarly, mean crushing force exhibits an initial rise from 137 kN to 161 kN before decreasing to 103 kN. This is because, in IFAFSDTs with a relatively low L, the aluminum foam core enters the densification stage earlier during the impact process. This earlier densification enhances load-carrying performance[15] and inhibits further deformation of aluminum alloy tubes[54]. As the height increases, the volume of aluminum foam filler increases, and the contact area between the aluminum foam core and the inner/outer aluminum alloy tubes increases, resulting in the enhanced interaction between sandwich core and aluminum alloy tubes[55]. Consequently, within a specific height range, the load-bearing performance continues to improve. However, as the height of the IFAFSDTs further increases, in accordance with Euler's equation for stable load-bearing capacity of tubes in engineering mechanics, longer rods or tubes are more susceptible to buckling or failure under axial loading, as shown in Eq. (9):

$$F_{cr} = \frac{\pi^2 EI}{H^2} \tag{9}$$

where F_{cr} is ultimate bearing capacity before deformation of tubes, E is elastic modulus. I is the cross-sectional moment of inertia, which is only related to the inner and outer diameters of the tubes, and H is the height of specimen. According to Eq. (9), when inner and outer diameters of tubes are constant, the ultimate bearing capacity decreases with the increase of H before buckling occurs. Moreover, when the height of IFAFSDTs is high, aluminum foam core does not undergo earlier densification during the progressive collapse, which reduces the impact of aluminum foam densification on the impact resistance performance, thereby lowering the impact loads[56]. Although the IFAFSDTs with L of 1.5 exhibit significantly lower peak and mean stresses than those with L of 1 and 1.25, they demonstrate exhibit longer energy-absorbing stroke, representing an effective strategy for improving impact resistance safety.

The effect of L on the energy absorption performance of IFAFSDTs is presented in Fig. 13. As L increases, the total absorbed energy and energy absorption capacity first increase

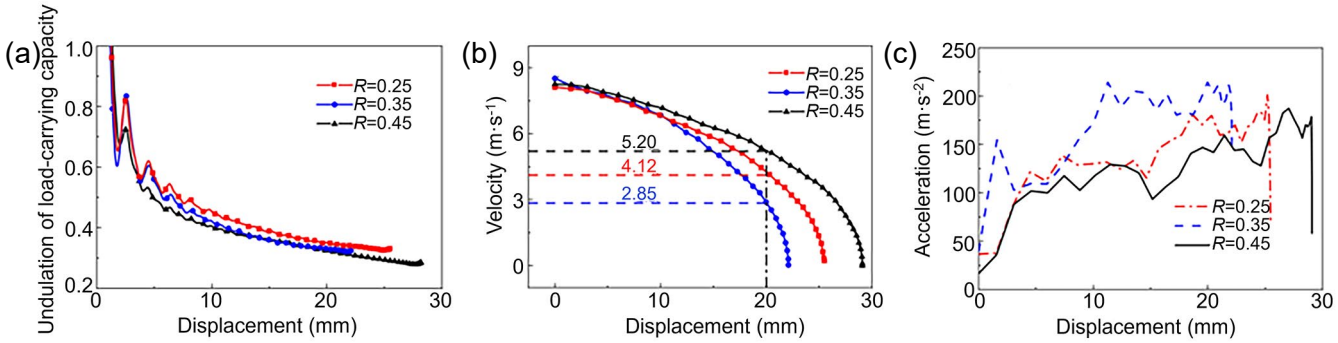

Fig. 11: Effect of *R* on crashworthiness of IFAFSDTs: (a) undulation of load-carrying capacity; (b) deformation velocity; (c) deformation acceleration

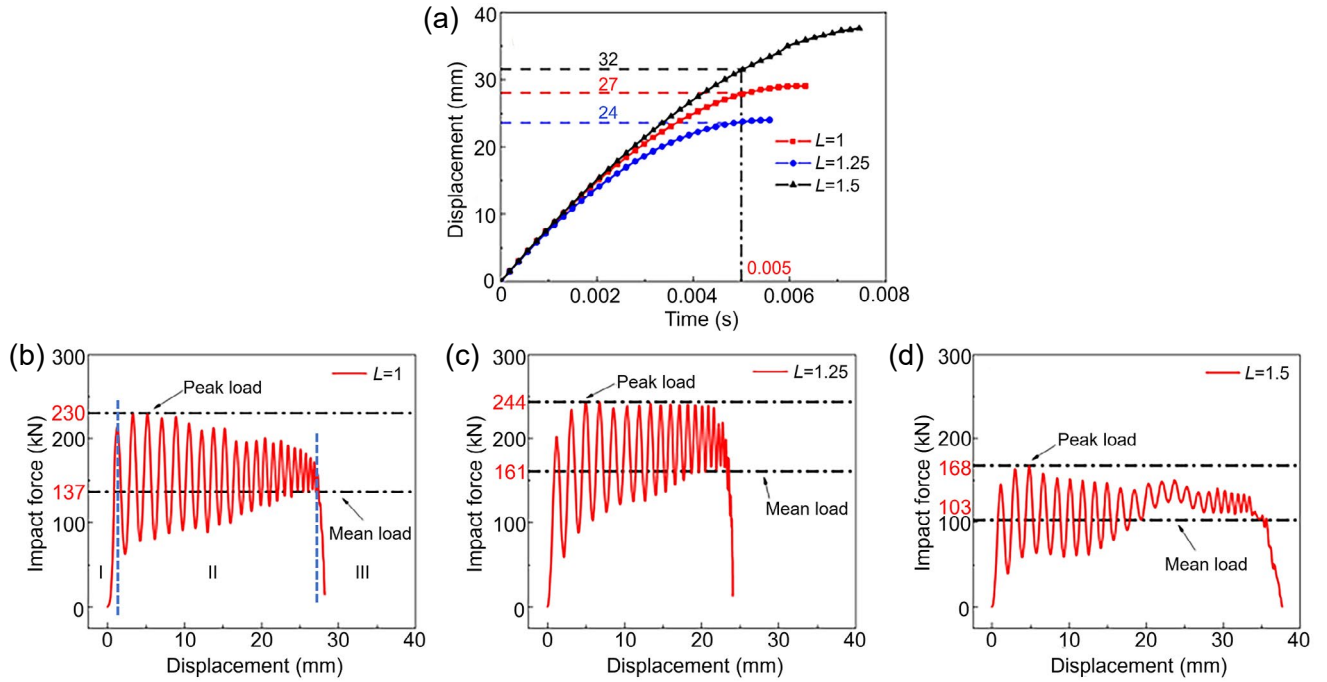

Fig. 12: Effect of *L* on deformation displacement and impact force of AFSDTs: (a) displacement-time curves; (b–d) impact force-displacement curves

and then decrease. When axial displacement is 20 mm, specimens with L of 1, 1.25, and 1.5 exhibit total impact energy absorption values of 2,713 J, 3,171 J, and 1,958 J, respectively. The energy absorption capacities with strain of 0.3 are measured as 35.7 MJ·m^{-3}, 43.3 MJ·m^{-3}, and 27.6 MJ·m^{-3}. Therefore, under the same displacement or strain, IFAFSDTs with L of 1.25 exhibit superior energy absorption performance. Figure 13(b) shows IFAFSDTs with L=1.5 experience a strain of 0.42 after impact process, with an axial displacement of about 38 mm [Fig. 13(a)], which is greater than that of the samples with L=1 and 1.25. Although the energy absorption capacity of IFAFSDTs with L=1.5 is lower than that of samples with L=1 and 1.25, due to their maximum height, the volume of the undeformed region is the largest, and they possess the greatest potential for further energy absorption after impact[57, 58].

The effect of L on the load-carrying capacity of IFAFSDTs during drop-weight impact is illustrated in Fig. 14(a). Load fluctuation of IFAFSDTs is high during the initial impact stage and then gradually decreases. Samples with L=1.25 exhibit the lowest load-carrying capacity throughout the impact process. The effect of L on the deformation velocity of IFAFSDTs during axial impact is illustrated in Fig. 14(b). As L increases, the reduction of velocity first increases and then decreases. With axial deformation displacement of 20.0 mm, the deformation velocity for the three specimens is 5.20 m·s^{-1}, 3.51 m·s^{-1}, and 6.20 m·s^{-1}, respectively, representing reductions of 41.2%, 60.1%, and 29.9% from the initial velocity. The effect of L on the deformation acceleration of IFAFSDTs is shown in Fig. 14(c). When IFAFSDTs subject to impact, the deformation acceleration rises rapidly to a certain value and then fluctuate at a higher level and a lower amplitude, indicates that these samples all have a stable buffering process[49]. Specimens with L=1.25 exhibit the highest deformation acceleration, indicating superior crashworthiness. However, excessively high deformation acceleration may pose a risk, causing the protected individual to experience significant velocity change in a short time and potentially resulting in injury[59].

The peak crushing force and energy absorption capacity of IFAFSDTs are approximately 1.6 and 2 times higher than those of CAFTs with the same sizes (L=1)[33]. This enhancement is attributed to the addition of an inner tube and the good metallurgical bonding between aluminum foam core and inner/outer tubes, which enables IFAFSDTs to have high initial stiffness and peak crushing force, significantly improving the resistance to impact deformation. Thus, the mechanical response of IFAFSDTs under impact differs from that of structures with mechanical interlocking or adhesive bonding[26, 60, 61]. The deformation and tearing of metallurgical interface constitute a unique energy absorption mechanism for IFAFSDTs, further enhancing the energy absorption performance.

3.5 Deformation and failure mechanism

When drop hammer contacts with the specimen, one end of IFAFSDTs initially undergoes buckling deformation during impact process. As impact process progresses, the other end also experiences the same type of deformation. Finally, non-axisymmetric buckling deformation occurs in middle section of the sample. Under high-speed impact, the Plateau boundaries of aluminum foam gradually collapse and fracture, resulting in IFAFSDTs being compacted[62].

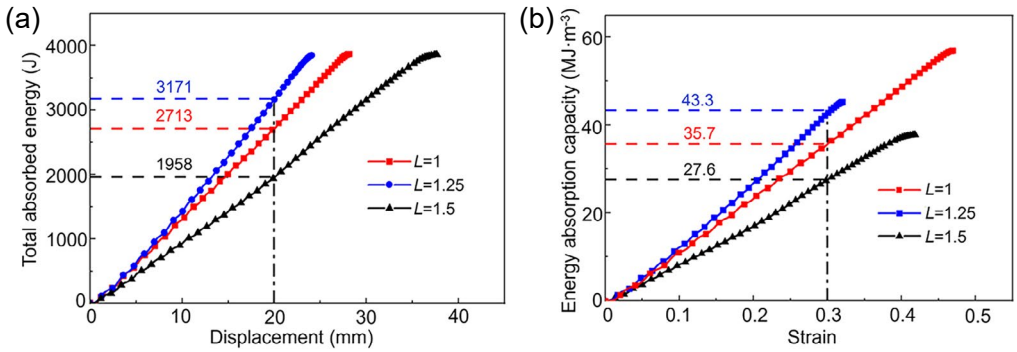

Fig. 13: Effect of L on energy absorption performance of IFAFSDTs: (a) total energy absorption; (b) energy absorption capacity

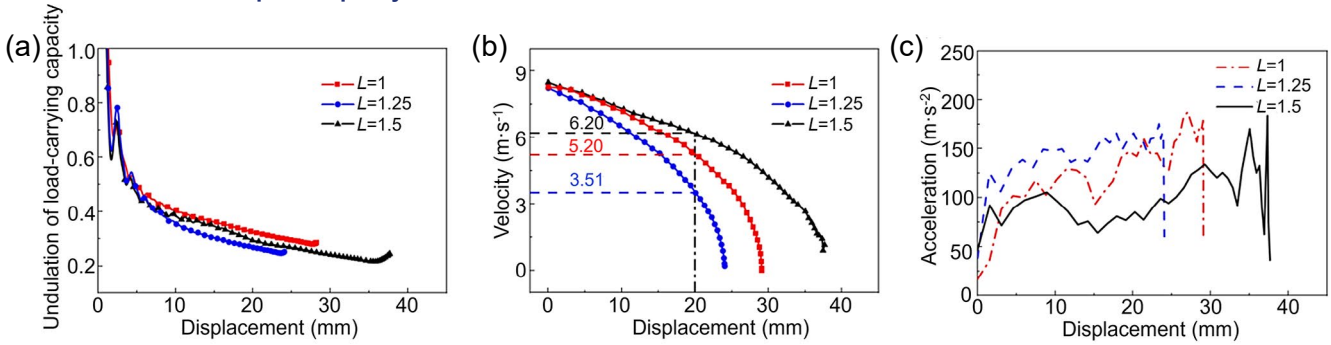

Fig. 14: Effect of L on crashworthiness of IFAFSDTs: (a) undulation of load-carrying capacity; (b) deformation velocity; (c) deformation acceleration

Aluminum foam can reduce the maximum axial displacement, enhance the overall energy absorption capacity, and prevent a sharp increase in impact force when IFAFSDTs reach densification[63]. The interaction between the aluminum foam core and the solid aluminum tubes also significantly improves the impact performance[64]. Compared with CAFTs, the deformation and damage extent of IFAFSDTs under drop hammer impact are lower, and their impact resistance is superior. This is attributed to the metallurgical bonding between the foam core and inner/outer aluminum alloy tubes, which enhances the overall deformation resistance and stiffness[65, 66]. Additionally, the inner tube improves the axial impact resistance and energy absorption performance of the aluminum foam-filled tube structure, effectively stabilizes its deformation mode, and makes the energy absorption and impact resistance processes more stable[67].

The buckling deformation of IFAFSDTs with the same height and low R values under drop hammer impact initially occurs near the impact end. Subsequently, impact stress is transmitted through foam core and solid tubes to the base plate. Under the reaction force of the base plate, buckling deformation occurs at the bottom of the IFAFSDTs. As drop hammer continues to move, fragments generated during the densification of the sandwich core and the deformed regions move radially along the tube[19], forming buckling in the middle section of IFAFSDTs, as shown in Fig. 15. At elevated R values, the volume of the solid aluminum tube increases. Due to the fast transmission of stress waves in high-density aluminum alloy tube[68], the impact load is rapidly transmitted through the solid aluminum tubes to the bottom of the IFAFSDTs, leading to the initial formation of buckling deformation near the base plate, followed by the formation of wrinkles in the upper and middle sections, as shown in Fig. 15(c). Due to the varying degrees of densification in different regions of the aluminum foam core during compression, the resulting wrinkles are not perfectly symmetrical rings. Both inner and outer tubes exhibit buckling deformation. The deformation degree of the inner tube is greater, and cracks appear at the folds. This indicates that the inner tube bears a significant portion of the impact load, effectively enhancing the overall impact resistance of the structure[64]. When R=0.25, the wrinkles in the middle section of the specimen are not pronounced, suggesting that a higher filling of aluminum foam suppresses the buckling deformation of the outer tube. When R=0.35, localized cracks appear in the outer tube of the specimen. The peak impact load and average stress are higher at R=0.35, which is the cause of the crack formation.

When L=1, the height of IFAFSDTs is low, and the impact velocity is relatively high when the hammer comes into contact with the sample, leading to localized crushing on the impact end. When L increases from 1 to 1.25, the buckling deformation mode of IFAFSDTs transitions from initial buckling at the bottom to nearly simultaneous buckling at both the top and bottom, as shown in Fig. 16. This indicates that an increase in the height of IFAFSDTs enhances the plasticity and deformation capacity. The stress wave is rapidly transmitted through the

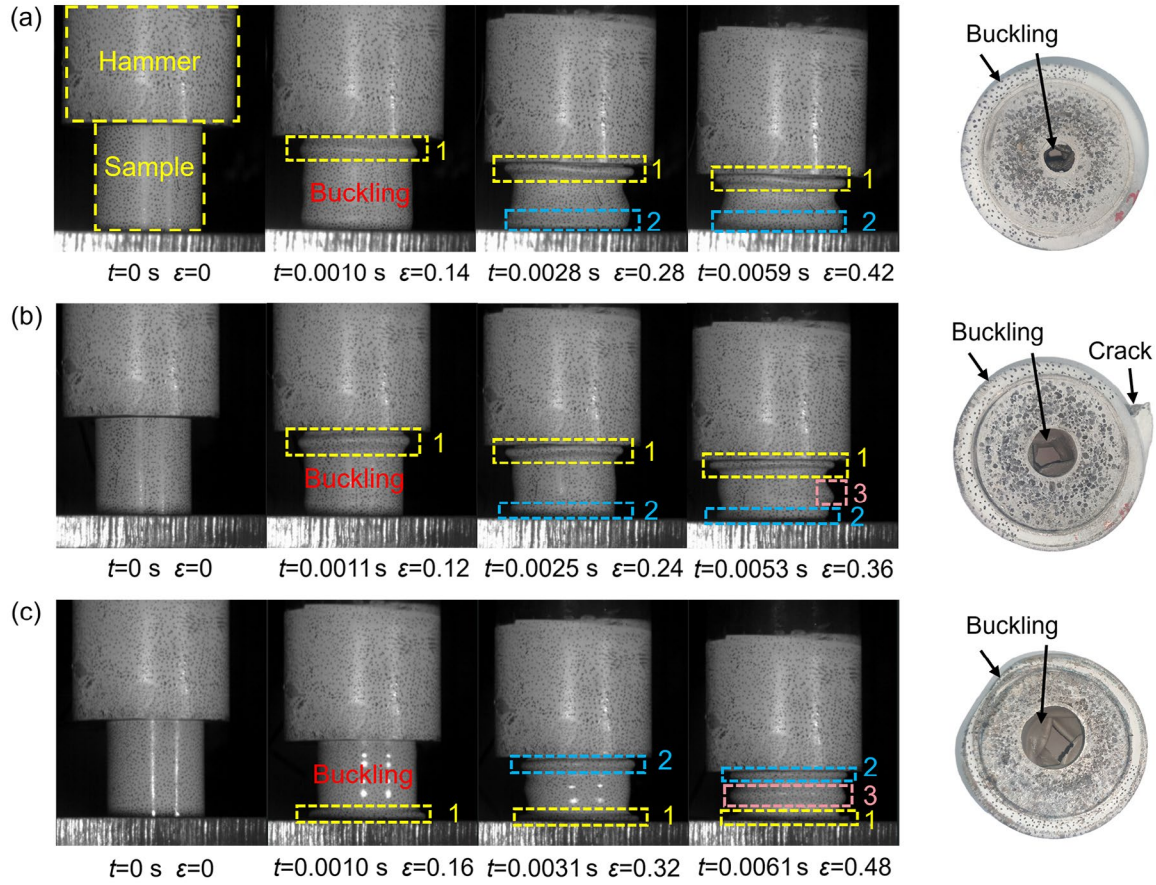

Fig. 15: Impact process and failure mode of IFAFSDTs with different R: (a) R=0.25; (b) R=0.35; (c) R=0.45

solid aluminum alloy tube to the bottom plate, and the reaction force from the bottom plate causes buckling deformation in the lower part of the tube. When L=1.5, the time for the stress wave to reach the bottom becomes longer. And due to the inertial effect, the impact end yields first, while the support end undergoes plastic deformation initially until the stress wave propagates to the support end[69]. Therefore, the position where buckling deformation first occurs is related to the filling amount of aluminum foam, inertia effect, and stress wave transmission speed[70].

In conclusion, the outer tube of all IFAFSDTs shows an axisymmetric circular buckling deformation mode, which exhibits high energy absorption efficiency[71]. This is attributed to the restriction of inward lateral displacement by the aluminum foam core and inner tube, ensuring the stability of the outer tube deformation[18]. Under drop hammer impact, the inner tube undergoes severe wall deformation characterized by an asymmetric diamond mode where folds are compressed against each other, ultimately leading to cracks. The deformation of the aluminum foam core is constrained by inner and outer tubes, absorbing energy through a densification process under impact stress and providing support to the outer tube. Compared to FFTs and CAFTs, the metallurgical bonding in IFAFSDTs results in more significant interactions between the core and tube walls[72], which endows IFAFSDTs with superior energy absorption performance under identical drop hammer impact conditions.

To further investigate the deformation and failure mechanism, FE simulation was conducted on the drop-weight impact process. Simulation results are in good agreement with experimental results, as shown in Fig. 17. From stress cloud map, when ε=0.125, the stress is mainly concentrated on the inner and outer tube, while aluminum foam core has no obvious deformation. Then, obvious buckling deformation appears under ε=0.25. Simulation results show that, the stress on inner and outer tubes further increases, the foam core near the impact end exhibits obvious deformation and cracks appear on some cell walls. When strain is 0.375, the sample has axisymmetric and non-axisymmetric circular folds. The non-axisymmetric circular fold is caused by local inhomogeneity of aluminum foam core. Cracks appear in both inner and outer tubes. The foam core has large deformation and stress concentration with some cell walls broken. When strain reaches 0.5, a collapse zone develops along the stress concentration and fracture site of the inner tube. Subsequently, both the inner and outer tubes fracture, resulting in the overall failure[73].

3.6 Energy absorption forms during drop-weight impact process

IFAFSDTs are different in the energy absorption modes from those prepared by placing the foam core directly into alloy tube[26, 74] or bonding the foam core to the alloy tube[75, 76]. This is due to the high bonding strength of metallurgical bonding interface, which contributes to improved energy absorption efficiency[60]. The energy absorption mechanism of IFAFSDTs in impact process is manifested in the following four forms: (1) energy absorption of outer tube through the axisymmetric

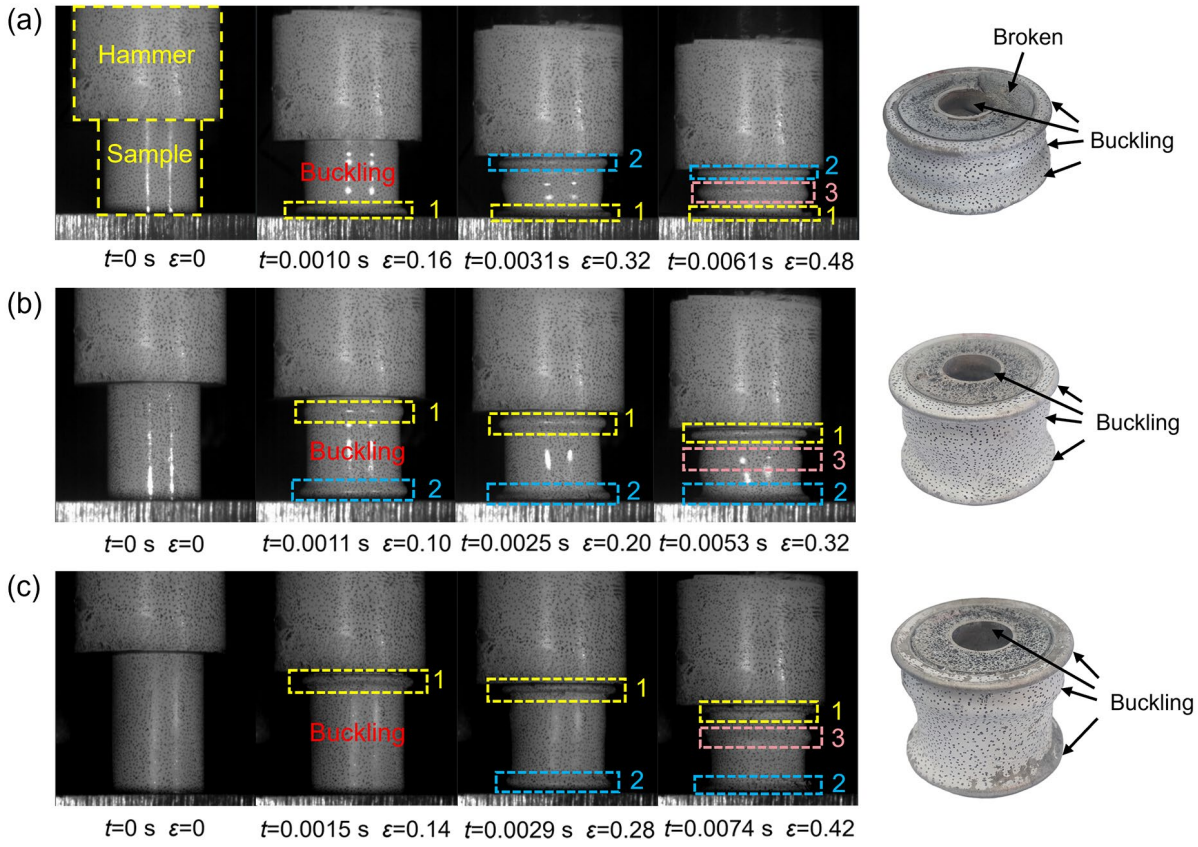

Fig. 16: Impact process and failure mode of IFAFSDTs with different L: (a) L=1.0; (b) L=1.25; (c) L=1.5

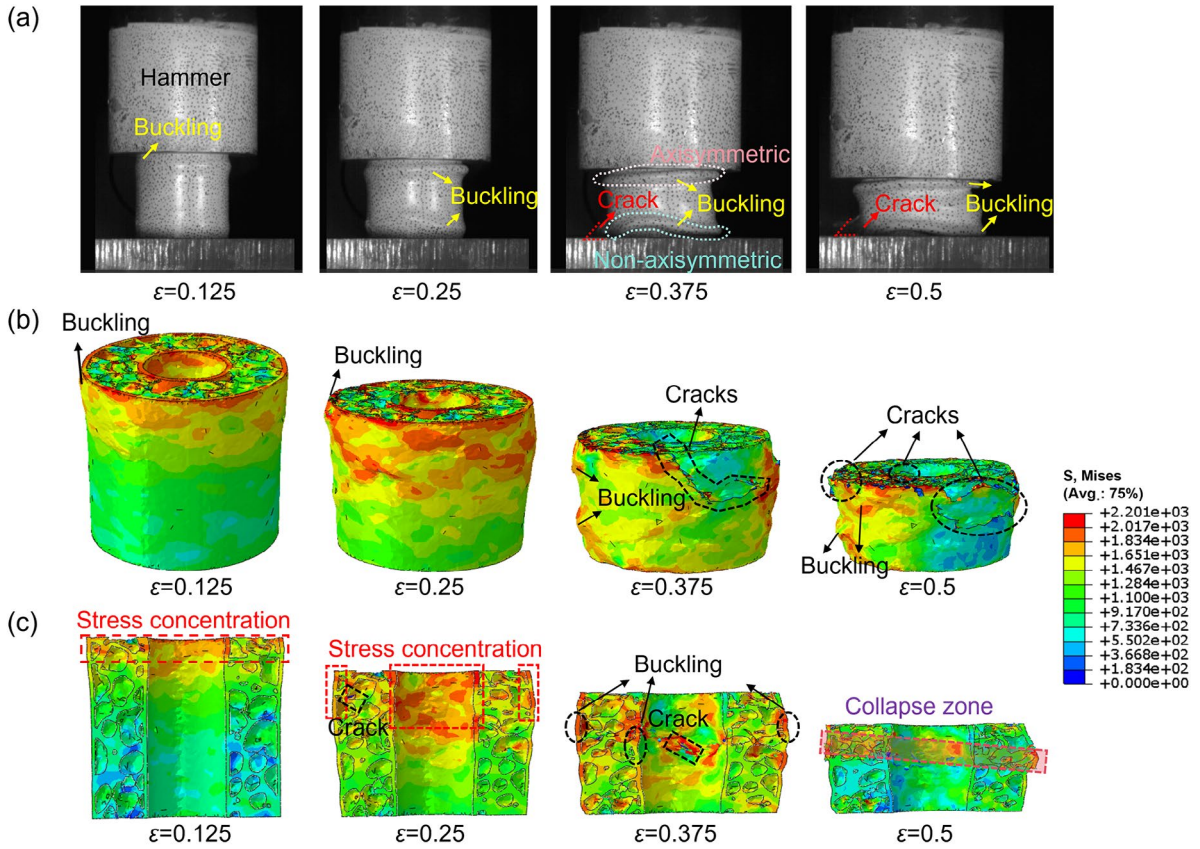

Fig. 17: Deformation and failure mechanism of IFAFSDTs: (a) experimental impact process; (b) and (c) stress cloud map

buckling deformation mode; (2) energy absorption of inner tube through diamond deformation mode; (3) energy absorption of aluminum foam core through deformation, disruption, and densification; (4) energy absorption through the damage and tearing of the metallurgical bonding interface. As shown in the SEM analysis in Fig. 18, the microscopic energy absorption mechanism of aluminum foam core can be further divided into three forms: (1) energy absorbed through deformation and collapse of cells, while the initiation and propagation of cracks around collapsed cells further enhance energy dissipation; (2) energy absorption via grain plastic deformation, manifested by the elongation of grains along a specific direction; (3) partial areas inside the nodes and cell walls absorb energy through the intergranular fracture mechanism.

At impact and support ends of IFAFSDTs, the collapse of cell walls leads to the interconnection of adjacent cells [(Figs. 18(a) and (b)], and the densification of the aluminum foam core absorbs impact energy. Cells are strongly compressed and accompanied by crack formation in the severely deformed regions such as impact end, support end, and the extruded region of the aluminum alloy tube [Fig. 18(d)]. Due to the coordinated effect of polycrystalline deformation, grains around collapsed cells undergo significant elongation along the compression direction. In the middle area of IFAFSDTs, the deformation of foam aluminum is relatively mild, cells are relatively intact. Grains near the walls of aluminum alloy tube and at the nodes have no obvious deformation, with only local microcracks distributed along the grain boundaries that rarely propagate into the grains [Fig. 18(e)]. In the transition region between two ends and the middle is a medium deformation area. Grains near the wall of tube and at nodes are elongated in different directions [Figs. 18(f) and (g)]. The grain elongation directions in the lower middle (blue solid line box) and lower regions (green dashed line box) are indicated by arrows.

To further explain the grain deformation and crack propagation mechanism in aluminum foam core, the forces applied to different regions of the foam core were analyzed. Taking the impact end as an example [Fig. 19(a)], the vertical impact force F can be decomposed into F_1 and F_2. F_1 drives the deformation of the cells and elongates the surrounding grains along the direction of deformation [Fig. 19(b)]. F_2 causes the initiation and propagation of cracks along the second phase at the grain boundaries. In the region of medium deformation, due to metallurgical bonding at the interface, the buckling deformation of the outer tube drives the aluminum foam at the wall outward along the diameter. Upon impact, the inner tube deforms both inward and outward. When deformed outward, inner tube pushes aluminum foam outward. Therefore, in the lower middle region [Fig. 19(d)], the combined impact and support forces F, along with the inner and outer tube forces (T_1 from the outer tube buckling and T_2 generated by the inner tube deformation) constitute the total force F_{total}, causing grains to elongate in a specific direction. In the lower part of IFAFSDTs, the support force is larger and the combined force in the vertical direction is N. Under the combined effect of N, T_1, and T_2, grains elongate along the deformation direction shown in Fig. 19(e). Therefore, the difference in deformation modes of aluminum foam core mainly depends on impact and

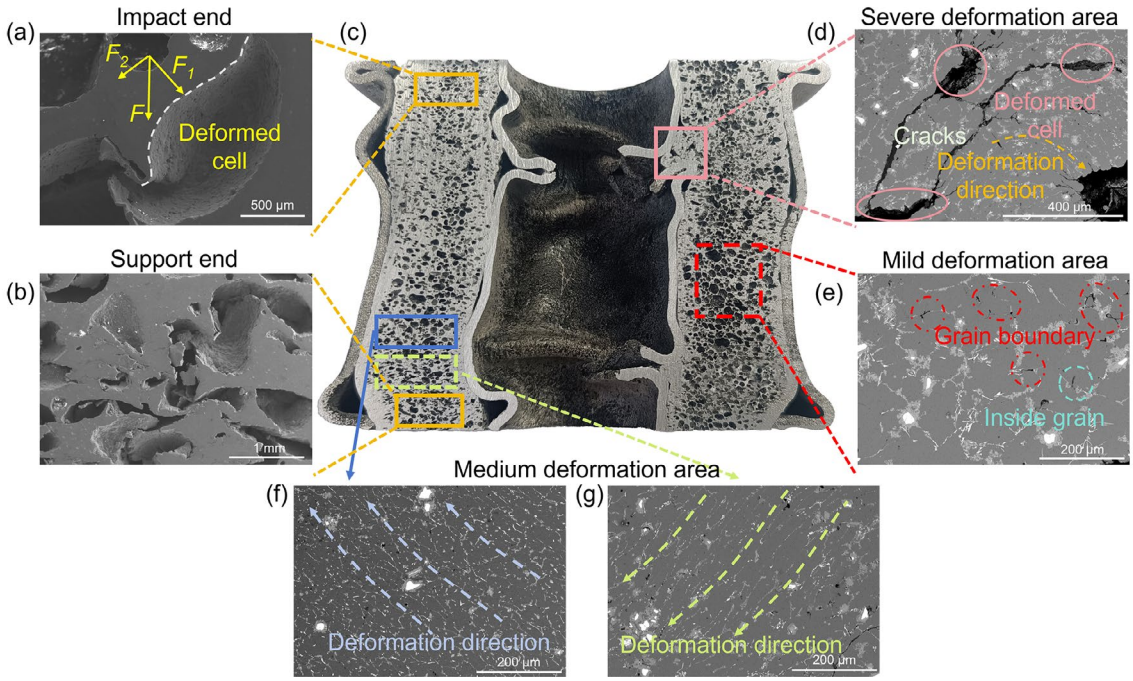

Fig. 18: Microstructures of aluminum foam core after impact: (a) impact end; (b) support end; (c) sampling positions; (d) severe deformation area; (e) mild deformation area; (f) and (g) medium deformation area

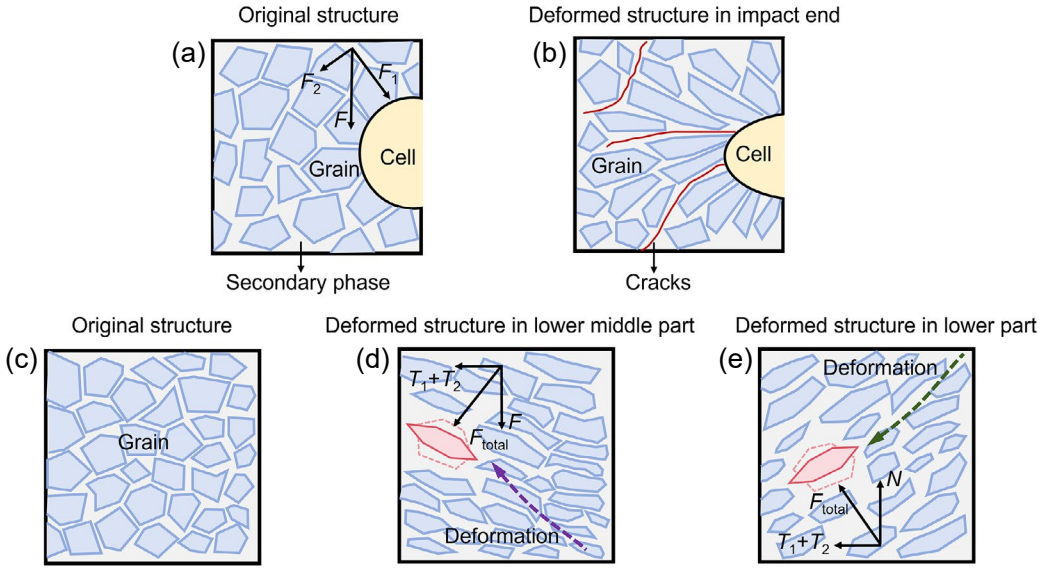

Fig. 19: Grain deformation and crack propagation mechanism: (a) original structure and force analysis in impact end; (b) deformed structure in impact end; (c) original structure in medium deformation area; (d) deformed structure and force analysis in lower middle part; (e) deformed structure and force analysis in lower part

support forces, the synergistic deformation of inner and outer tubes, and the strength of metallurgical bonding interface.

Subsequently, the three energy absorption mechanisms of aluminum foam core under dynamic impact were quantitatively evaluated. The energy absorbed by cell wall deformation and collapse (W_{cell}) was calculated by Gibson-Ashby foam material theory combined with unit cell model[77, 78], and the dynamic enhancement factor $C(\dot{\varepsilon})$ was used to characterize the strain rate effect[79], which was calibrated through drop-weight hammer impact test. For the energy absorption mechanism of grain plastic deformation, based on the theory of dislocation energy storage[80], the energy absorbed during grain elongation (W_{disl}) is quantified by calculating the dislocation density after deformation. This energy is mainly converted into grain boundary slip or rotation, dislocation proliferation and movement, and lattice elastic energy storage[81, 82]. The energy absorbed by intergranular fracture (W_{GB}) depends on the fracture surface energy and grain boundary characteristics[83]. The key parameters, average grain size D and intergranular fracture ratio f_{GB}, were obtained through statistical analysis of SEM images using ImageJ software.

$$W_{cell} = \sigma_y \varepsilon_p (1-P) C(\dot{\varepsilon}) \tag{10}$$

$$W_{disl} = \frac{1}{2} G \boldsymbol{b}^2 \rho \tag{11}$$

$$W_{GB} = \gamma A_{GB} C(\dot{\varepsilon}) f_{GB} / V \tag{12}$$

where σ_y is the yield strength of the matrix alloy, ε_p represents the densification strain of the foam core, P is porosity, G is the

matrix shear modulus, $\boldsymbol{b}$ is the Burgers vector, ρ denotes the dislocation density, γ_{GB} is the grain boundary fracture energy per unit area. According to Griffth's theory, the relationship between the fracture energy γ and the surface energy γ_s and grain boundary energy γ_{GB} can be expressed as: $\gamma=2\gamma_s-\gamma_{GB}$[84, 85]. A_{GB} is the total area of fractured grain boundaries, f_{GB} is the proportion of intergranular fracture, and V represents the volume of intergranular fracture.

Based on existing literature reports and experimental data, the relevant parameters were obtained, as shown in Table 2. The energy absorption capabilities of three mechanisms are compared and quantified, as shown in Fig. 20. It can be seen that the deformation and collapse of the cell wall are the main source of energy absorption of aluminum foam core.

Table 2: Parameters used for calculating energy absorption

σ_y (MPa)	ε_p	C ($\dot{\varepsilon}$)	G (GPa)	b (nm)	ρ (m^{-2})	γ ($J\cdot m^{-2}$)	D (μm)	f_{GB}
82.354[30]	0.42	3.6	27[86]	0.286	10^{14}–10^{16}[87]	1.9[84]	45.8	0.2

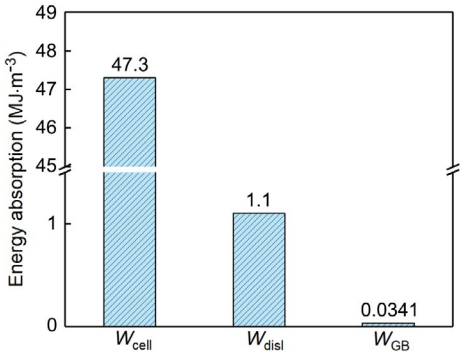

Fig. 20: Energy absorption capacity of different energy absorption mechanisms in foam core

4 Conclusions

This study employed the improved melt foaming method to accomplish the integral preparation of IFAFSDTs. The axial impact resistance of IFAFSDTs was systematically evaluated through drop-weight impact testing, with particular emphasis on the effect of diameter ratio (R) and aspect ratio (L). Furthermore, deformation characteristics and failure mechanisms of IFAFSDTs were analyzed, and principal findings of this work can be summarized as follows:

(1) IFAFSDTs with metallurgical bonding between the aluminum foam core and inner/outer aluminum alloy tubes were fabricated using integrated forming method. Inner/outer tubes maintain their structural integrity without deformation, while the aluminum foam core exhibits a uniform pore structure distribution.

(2) The load-carrying capacity and energy absorption performance of IFAFSDTs increase first and then decrease with the increase of R and L. IFAFSDTs with a high R or L value exhibit relatively stable load fluctuations during the impact process, and the deformation acceleration and impact stress are lower. IFAFSDTs with a height of 60 mm and R=0.35, as well as those with all inner diameter of 27 mm and L=1.25, exhibit superior axial impact resistance performance.

(3) During impact process, outer aluminum alloy tube exhibits an axisymmetric circular progressive buckling deformation mode, while inner tube follows an asymmetric diamond mode, aluminum foam core undergoes the densification process, and metallurgical bonding interface is damaged. There is a strong interaction between aluminum foam core and inner/outer tubes, effectively constraining excessive deformation of the tubes. Furthermore, the sequence and location of buckling deformation and wrinkling formation are influenced by multiple factors, including the volume of aluminum foam, inertia effect, and stress wave transmission speed.

(4) Aluminum foam core absorbs impact energy of falling weight through modes of pore structure deformation, crack propagation, and grain deformation. The differences in the energy absorption modes mainly depend on the dynamic balance between the impact and the support force, the deformation behavior of the inner and outer tubes, and the bonding strength of the metallurgical interface. This leads to different energy absorption modes and microstructures after deformation at different positions.

Acknowledgments

This work was financially supported by the National Natural Science Foundation of China (No. 52575374), the Hebei Provincial Natural Science Foundation General Project (No. 2025202207), the Civil-Military Science and Technology Collaborative Innovation Special Project (No. 22351003D), the Central Guidance Local Science and Technology Development Fund Project (No. 246Z1029G), and the Hebei Province Higher Education Science Technology Research Project (No. ZD2020191).

Conflict of interest

The authors declare that they have no known competing financial interests or personal relationships that could have appeared to influence the work reported in this paper.

References

[1] Zhao C, Zhong J, Wang H, et al. Impact behaviour and protection performance of a CFRP NPR skeleton filled with aluminum foam. Mater. Design., 2024, 246: 113295.
[2] Wattad O and Grisaro H Y. On the efficiency of uniform aluminum foam as energy-absorbing sacrificial cladding for structural blast mitigation. Int. J. Mech. Sci., 2024, 308: 118047.

[3] Wang N, Zhu M, Yang R, et al. Cell size controlling of closed-cell aluminum foams. J. Mater. Res. Technol., 2025, 36: 1294–1313.
[4] Zhang Z, Feng H, Xu T, et al. Compression performances of integral-forming aluminum foam sandwich. Compos. Struct., 2022, 283: 115090.
[5] Zhang Y, He S Y, Liu J G, et al. Density gradient tailoring of aluminum foam-filled tube. Compos. Struct., 2019, 220: 451–459.
[6] Song J, Xu S, Xu L, et al. Experimental study on the crashworthiness of bio-inspired aluminum foam-filled tubes under axial compression loading. Thin. Wall. Struct., 2020, 155: 106937.
[7] Mirbagheri S M H and Salehi M. Complementary and normalized energies during static and dynamic uniaxial deformation of single and multi-layer foam-filled tube. J. Sandw. Struct. Mater., 2022, 24: 1470–1490.
[8] Salehi M, Mirbagheri S, Ramiani A J. Efficient energy absorption of functionally-graded metallic foam-filled tubes under impact loading. T. Nonferr. Metal. Soc., 2021, 31(1): 92–110.
[9] Movahedi N and Linul E. Quasi-static compressive behavior of the ex-situ aluminum-alloy foam-filled tubes under elevated temperature conditions. Mater. Lett., 2017, 206: 182–184.
[10] Li Z, Yu J, Guo L. Deformation and energy absorption of aluminum foam-filled tubes subjected to oblique loading. Int. J. Mech. Sci., 2012, 54(1): 48–56.
[11] Sun G, Chen D, Wang H, et al. High-velocity impact behaviour of aluminium honeycomb sandwich panels with different structural configurations. Int. J. Impact. Eng., 2018, 122: 119–136.
[12] Gao X, Zhang M, Huang Y, et al. Experimental and numerical investigation of thermoplastic honeycomb sandwich structures under bending loading. Thin. Wall. Struct., 2020, 155: 106961.
[13] Jafarian B and Rezvani M J. An experimental investigation on energy absorption of thin-walled bitubal structures by inversion and axial collapse. Int. J. Mech. Sci., 2017, 126: 270–280.
[14] Sun G, Wang Z, Yu H, et al. Experimental and numerical investigation into the crashworthiness of metal-foam-composite hybrid structures. Compos. Struct., 2019, 209: 535–547.
[15] Linul E and Khezrzadeh O. Axial crashworthiness performance of foam-based composite structures under extreme temperature conditions. Compos. Struct., 2021, 271: 114156.
[16] Garai F, Beres G, Weltsch Z. Development of tubes filled with aluminium foams for lightweight vehicle manufacturing. Mat. Sci. Eng. A, 2020, 790: 139743.
[17] Rogala M, Ferdynus M, Gawdzińska K, et al. The influence of different length aluminum foam filling on mechanical behavior of a square thin-walled column. Materials, 2021, 14(13): 3630.
[18] Duarte I, Krstulović-Opara L, Vesenjak M. Axial crush behaviour of the aluminium alloy in-situ foam filled tubes with very low wall thickness. Compos. Struct., 2018, 192: 184–192.
[19] Hangai Y, Otazawa S, Utsunomiya T. Aluminum alloy foam-filled aluminum tube fabricated by friction stir back extrusion and its compression properties. Compos. Struct., 2018, 183: 416–422.
[20] Taherishargh M, Vesenjak M, Belova I, et al. In situ manufacturing and mechanical properties of syntactic foam filled tubes. Mater. Design., 2016, 99: 356–368.
[21] Chen Y, Hou S, Fu K, et al. Low-velocity impact response of composite sandwich structures: Modelling and experiment. Compos. Struct., 2017, 168: 322–334.
[22] Tarlochan F, Ramesh S, Harpreet S. Advanced composite sandwich structure design for energy absorption applications: Blast protection and crashworthiness. Compos. Part B-Eng., 2012, 43(5): 2198–2208.
[23] Wang Y, Zhang R, Liu S, et al. Energy absorption behaviour of an aluminium foam-filled circular-triangular nested tube energy absorber under impact loading. Structures, 2021, 34: 95–104.
[24] Guo L and Yu J. Dynamic bending response of double cylindrical tubes filled with aluminum foam. Int. J. Impact. Eng., 2011, 38(2): 85–94.
[25] Ni X H, Zhang X G, Han D, et al. Aluminum foam-filled auxetic double tubular structures: Design and characteristic study. Mech. Adv. Mater. Struc., 2024, 31(15): 3377–3388.
[26] Yan S, Jiang Y, Deng Y, et al. Energy absorption characteristics of aluminum foam-filled corrugated tube under axial compression loading. Thin. Wall. Struct., 2024, 195: 111333.
[27] Li X, Liu Y, Ye J, et al. Innovative surface modification of TiH_2 to fabricate aluminum foam with enhanced mechanical properties. Mater. Lett., 2018, 210: 350–353.
[28] Barode J, Aravind U, Bhogi S, et al. Mg and mg-based blowing agents for aluminum foam. Metall. Mater. Trans. B, 2021, 52(1): 292–304.
[29] Banhart J. Metal foams: Production and stability. Adv. Eng. Mater., 2006, 8(9): 781–794.
[30] Zhang Z, Liu N, Zhang Z, et al. Compression performances of composite aluminum foam tubes. Int. J. Mech. Sci., 2023, 242: 108039.
[31] Hui W, Bo L, Juan Y, et al. Thermal properties of closed-cell aluminum foams prepared by melt foaming technology. Trans. Nonferr. Metal. Soc., 2016, 26(12): 3147–3153.
[32] Duarte I, Vesenjak M, Krstulović-Opara L, et al. Manufacturing and bending behaviour of in situ foam-filled aluminium alloy tubes. Mater. Design, 2015, 66: 532–544.
[33] Wang J, Xu X, Zhang Z, et al. Axial impact performances of composite aluminum foam tubes. Adv. Eng. Mater., 2024, 26(20): 2400897.
[34] San Ha N and Lu G. A review of recent research on bio-inspired structures and materials for energy absorption applications. Compos. Part B-Eng., 2020, 181: 107496.
[35] San Ha N, Pham T M, Tran T T, et al. Mechanical properties and energy absorption of bio-inspired hierarchical circular honeycomb. Compos. Part B-Eng., 2022, 236: 109818.
[36] Wang W, Wang Y, Zhao Z, et al. Numerical simulation and experimental study on energy absorption of foam-filled local nanocrystallized thin-walled tubes under axial crushing. Materials, 2022, 15(16): 5556.
[37] Xie S, Zhang J, Liu X, et al. A reinforced energy-absorbing structure formed by combining multiple aluminum foam-filled open-hole tubes. Int. J. Mech. Sci., 2022: 224.
[38] Hu H, Lai Z, Ding G. Influence of surface wettability on heat transfer and pressure drop characteristics of wet air in metal foam under dehumidifying conditions. Int. J. Therm. Sci., 2019, 135: 331–343.
[39] Wang N, Chen X, Maire E, et al. Study on cell deformation of low porosity aluminum foams under quasi-static compression by X-ray tomography. Adv. Eng. Mater., 2020, 22(10): 2000264.
[40] Kim S, Choi S, Ahn T Y, et al. Effect of space holder size on microstructure and mechanical properties of aluminum foam. Met. Mater. Int., 2025, 31: 2432–2442.
[41] Çıbıkçı K Ç and Yaman M. Experimental investigation of compressive behavior and vibration properties of layered hybrid foam formed by aluminum foam/EPS-filled syntactic foam. J. Mater. Sci., 2024, 59(8): 3636–3651.
[42] Liu N, Zhang Z, Xia X, et al. Local deformation on damping performance of integral-forming aluminum foam sandwich. Mater. Lett., 2022, 323: 132545.
[43] Zhang Z C, Zhang Z, Liu N, et al. Three-point bending performances of integral-forming aluminum foam sandwich. Mater. Design., 2023, 229: 111889.
[44] Mohan K, Yip T H, Idapalapati S, et al. Impact response of aluminum foam core sandwich structures. Mat. Sci. Eng. A, 2011, 529: 94–101.
[45] Zhang Y, Liu Q, He Z, et al. Dynamic impact response of aluminum honeycombs filled with expanded polypropylene foam. Compos. Part. B-Eng., 2019, 156: 17–27.
[46] Yamashita M and Gotoh M. Impact behavior of honeycomb structures with various cell specifications – numerical simulation and experiment. Int. J. Impact Eng., 2005, 32(1): 618–630.

[47] Duarte I, Vesenjak M, Krstulović-Opara L. Variation of quasi-static and dynamic compressive properties in a single aluminium foam block. Mat. Sci. Eng. A, 2014, 616: 171–182.
[48] Sun G, Li S, Liu Q, et al. Experimental study on crashworthiness of empty/aluminum foam/honeycomb-filled CFRP tubes. Compos. Struct., 2016, 152: 969–993.
[49] Yang H, Lei H, Lu G. Crashworthiness of circular fiber reinforced plastic tubes filled with composite skeletons/aluminum foam under drop-weight impact loading. Thin. Wall. Struct., 2021, 160: 107380.
[50] Linul E, Movahedi N, Marsavina L. The temperature effect on the axial quasi-static compressive behavior of ex-situ aluminum foam-filled tubes. Compos. Struct., 2017, 180: 709–722.
[51] Kao Y T, Amin A R, Payne N, et al. Low-velocity impact response of 3D-printed lattice structure with foam reinforcement. Compos. Struct., 2018, 192: 93–100.
[52] Kim S, Kim D G, Kim M, et al. Analyses of impact energy-absorbing performance of open-and closed-cell Al foams using modified split Hopkinson pressure bar. J. Alloys Compd., 2023, 965: 171349.
[53] Zhang Y, Sun L, Ren X, et al. Design and analysis of an auxetic metamaterial with tuneable stiffness. Compos. Struct., 2022, 281: 114997.
[54] Abdulqadir S, Alaseel B, Ansari M. Simulation of thin-walled double hexagonal aluminium 5754 alloy foam-filled section subjected to direct and oblique loading. Mater. Today., 2021, 42: 2822–2828.
[55] Djamaluddin F, Abdullah S, Ariffin A, et al. Optimization of foam-filled double circular tubes under axial and oblique impact loading conditions. Thin. Wall. Struct., 2015, 87: 1–11.
[56] Jensen Ø, Langseth M, and Hopperstad O. Experimental investigations on the behaviour of short to long square aluminium tubes subjected to axial loading. Int. J. Impact. Eng., 2004, 30(8): 973–1003.
[57] Saleem F, Li S, Cui S, et al. The strain rate and density dependence of the mechanical properties of closed-cell aluminum foam. Mat. Sci. Eng. A, 2023, 884: 145568.
[58] Xiang Y, Wang M, Yu T, et al. Key performance indicators of tubes and foam-filled tubes used as energy absorbers. Int. J. Appl. Mech., 2015, 7(4): 1550060.
[59] Reid J D, Hascall J A, Sicking D L, et al. Inertial effects during impact testing. Transport. Res. Rec., 2009, 2120(1): 39–46.
[60] Meriç D and Gedikli H. Multi-objective optimization of energy absorbing behavior of foam-filled hybrid composite tubes. Compos. Struct., 2022, 279: 114771.
[61] Kılıçaslan C. Numerical crushing analysis of aluminum foam-filled corrugated single-and double-circular tubes subjected to axial impact loading. Thin. Wall. Struct., 2015, 96: 82–94.
[62] Zhang J, Chen L, Wu H, et al. Experimental and mesoscopic investigation of double-layer aluminum foam under impact loading. Compos. Struct., 2020, 241: 110859.
[63] Lu J, Wang Y, Zhai X, et al. Impact behavior of a cladding sandwich panel with aluminum foam-filled tubular cores. Thin. Wall. Struct., 2021, 169: 108459.
[64] Li S, Guo X, Liao J, et al. Crushing analysis and design optimization for foam-filled aluminum/CFRP hybrid tube against transverse impact. Compos. Part B-Eng., 2020, 196: 108029.
[65] Zhang K H, Zhu X, Wang R, et al. Structural performance of aluminum foam-filled multi-cell steel tubes under axial impact. Structures, 2024, 69: 107527.
[66] Li X H, Yin Y, Zhu X, et al. Performance of hollow and aluminum foam-filled multi-cell thin-walled aluminum alloy tubes (6063-T5) under axial impact. Structures, 2023, 47: 1803–1821.
[67] Meng L, Zhai X, Wang Y. Investigation on lateral impact resistant performance of aluminum foam-filled 6082-T6 aluminum alloy circular tubes: Experimental and numerical study. Thin. Wall. Struct., 2023, 188: 110816.
[68] Wang X D, Yuan M N, Miao Y Z, et al. Stress wave propagation characteristics and impact resistance of laminated composites under impact loading. Mech. Adv. Mater. Struc., 2024, 31(8): 1822–1831.
[69] Duan Y, Chen X, Du B, et al. A predictive model for strain hardening and inertia effect of aluminum tubes filled with aluminum foam. Compos. Struct., 2022, 300: 116177.
[70] Movahedi N, Fiedler T, Taşdemirci A, et al. Impact loading of functionally graded metal syntactic foams. Mat. Sci. Eng. A, 2022, 839: 142831.
[71] Fyllingen Ø, Langmoen E, Langseth M, et al. Transition from progressive buckling to global bending of square aluminium tubes. Int. J. Impact. Eng., 2012, 48: 24–32.
[72] Duarte I, Krstulović-Opara L, Vesenjak M. Characterisation of aluminium alloy tubes filled with aluminium alloy integral-skin foam under axial compressive loads. Compos. Struct., 2015, 121: 154–162.
[73] Sahu S, Reddy T S, Reddy G J, et al. Low-velocity impact indentation rate sensitivity of aluminium foams. Mater. Today. Commun., 2020, 24: 101351.
[74] Zhuang W, Wang E, Zhang D, et al. Mesoscale study on the mechanical properties and energy absorption characteristics of aluminum foam-filled CFRP tubes under axial compression. Mech. Adv. Mater. Struc., 2024, 31: 10330–10346.
[75] Zhang C J, Yi F, Zhang X. Mechanical properties and energy absorption properties of aluminum foam-filled square tubes. Trans. Nonferr. Metal. Soc., 2010, 20: 1380–1386.
[76] Zhang Z, Huang L, Li B, et al. Design of a novel multi-walled tube-reinforced aluminum foam for energy absorption. Compos. Struct., 2021, 276: 114584.
[77] Hanssen A, Hopperstad O S, Langseth M, et al. Validation of constitutive models applicable to aluminium foams. Int. J. Mech. Sci., 2002, 44(2): 359–406.
[78] Gibson L J and Ashby M F. Cellular solids: Structure and properties, 2nd ed. Cambridge University Press, 1997.
[79] Deshpande V and Fleck N. High strain rate compressive behaviour of aluminium alloy foams. Int. J. Impact. Eng., 2000, 24(3): 277–298.
[80] Hull D and Bacon D J. Introduction to dislocations, 5th ed. Elsevier, Oxford, 2011.
[81] Sendrowicz A, Myhre A, Yasnikov I, et al. Stored and dissipated energy of plastic deformation revisited from the viewpoint of dislocation kinetics modelling approach. Acta. Mater., 2022, 237: 118190.
[82] Chen B, Zhu L, Xin Y, et al. Grain rotation in plastic deformation. Quantum Beam Science, 2019, 3(3): 17.
[83] Murr L E. Handbook of materials structures, properties, processing and performance. Springer, Switzerland, 2015.
[84] Ovid'Ko I A, Sheinerman A G, Aifantis E C. Stress-driven migration of grain boundaries and fracture processes in nanocrystalline ceramics and metals. Acta. Mater., 2008, 56(12): 2718–2727.
[85] Griffith A A. The phenomena of rupture and flow in solids. Philos. Trans. A, 1921, 221(582–593): 163–198.
[86] Smithells C J. Metals reference book, 5th ed. Elsevier, London, 2013.
[87] Hughes D and Hansen N. High angle boundaries formed by grain subdivision mechanisms. Acta. Mater., 1997, 45(9): 3871–3886.